Anomalous sudden drop of temperature-dependent Young's modulus of a plastically deformed duplex stainless steel

Xu Wang [a], Jianquan Wan [a,b], Jianbiao Wang [a], Linli Zhu [c], Haihui Ruan [a,*]

[a] Department of Mechanical Engineering, The Hong Kong Polytechnic University, Hom Hung, Kowloon, Hong Kong
[b] College of mechantronics and control engineering, Shenzhen university, Shenzhen 518060, Guangzhou Province, PR China
[c] Department of Engineering Mechanics, School of Aeronautics and Astronautics, Zhejiang University, Hangzhou 310027, Zhejiang Province, PR China

HIGHLIGHTS

- The anomalous sudden drop of modulus of a duplex stainless steel at 950 °C is found.
- The unexpected surge of the internal friction associate with the drop of modulus is observed.
- DSC results indicate an exothermal behavior associated with the recovery of the modulus.
- A physical picture of the crystal-amorphous-crystal two-step transition is conceived.

GRAPHICAL ABSTRACT
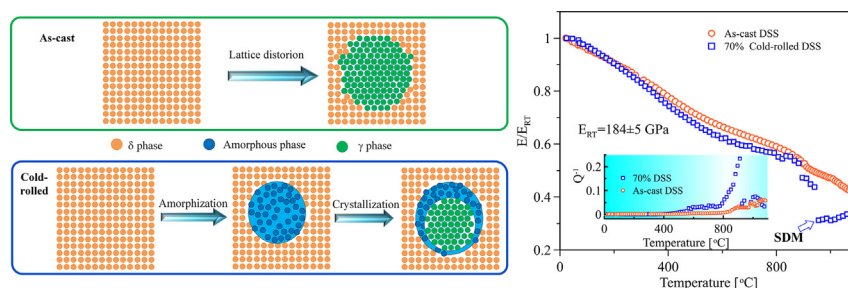
ARTICLE INFO

ABSTRACT

This work reports an anomalous and remarkable Sudden Drop of Modulus (SDM) associated with a precipitous surge of internal friction induced by the solid-state phase transformation (SSPT) in a severely cold-rolled duplex stainless steel (DSS). It is further shown that such a sudden drop does not appear if the DSS is not plastically deformed or if the severely rolled single-phase stainless steel is examined, indicating respectively that the phase growth or the recrystallization is not the cause. This anomaly occurs at the temperature between 930 and 950 °C, which is much lower than the solidus temperature of the DSS. And the results of differential scanning calorimetry (DSC) do not render any strong endothermic behavior at the temperature of SDM, excluding the possibility of pre-melting of some last solidified region. Based on these experimental results, we speculate that the SSPT in the severely deformed DSS may undergo a crystal-amorphous-crystal (CAC) two-step process, in which the intermediate amorphous phase with a low viscosity accounts for the sudden drop of the Young's modulus and the sudden surge of the internal friction. This amorphous phase is metastable, which gradually transforms to crystalline phase associated with a heat release and the slow recovery of stiffness.

1. Introduction

Solid-state phase transformation (SSPT) has broad applications in various fields [1–6] owing to the strong dependence of physical and

mechanical properties on microstructures. For example, by controlling SSPT, the optimized duplex structures can be achieved in ferrite-martensite dual phase steels for balancing strength and ductility [1] or in ferrite-austenite duplex stainless steels (DSS) for balancing mechanical and corrosive properties [2–4]. These applications explored basically the change of mechanical and physical properties when the transition from one phase to another has occurred. However, the kinetic

---

* Corresponding author.
  E-mail address: haihui.ruan@polyu.edu.hk (H. Ruan).

process of SSPT does not prominently influence the final properties and is generally not treated in a theoretical model. It is also extremely difficult to directly observe the details of the kinetic process of SSPT owing to the stringent requirement of spatial and temporal resolution. Therefore, how the phase transformation operates in material remains largely unrevealed. SSPT can broadly be classified into two types, namely diffusionless and diffusional transformation [5]. The former is relatively simple and has been more studied [6], because it only involves a finite lattice distortion induced by stress or temperature change, such as the stress-induced transformation in Partially Stabilized Zirconia (PSZ) [7] or in TRIP steel [8] and the martensite transformation when an austenitized plain carbon steel is rapidly cooled [9]. In contrast, diffusional transformation, such as the austenite-ferrite transformation in DSS [10,11], requires the radical change of composition and atomic arrangement, which could be very complex [12]. In addition, these two types of transformation may both occur in a material. For example, the decomposition of highly alloyed retained austenite in some tool steels involves the precipitation of various carbides and martensite transformation during cooling [13].

In 1897, Ostwald [14] observed sulfur crystallization and put forward the step rule that it is not the most stable but the least stable polymorph that crystallizes first. This step rule indicates polymorphism in a nucleation process, which was later observed experimentally in many systems, such as colloidal hard-sphere systems [15,16], polar stratospheric aerosols [17], and a silver bromide solution [18]. In SSPT, such a kinetic pathway is reminiscent of the Guinier–Preston zone and transient phase [19–21] in an early-state of precipitation. While it is well known that SSPT could be a process of transition among several transient crystalline phases, it has long been merely a conjecture that the transient phase could be completely amorphous [5,22,23]. The first experimental evidence of disordered transient phase in SSPT is shown by Peng et al. [5] in 2015, who observed that the amorphous arrangement of colloidal particles appeared first under the specific condition, in which the new crystalline phase subsequently nucleated, namely that the SSPT is featured by a crystal-amorphous-crystal (CAC) two-step process. Following this work, Pogatscher et al. [12] in 2016 observed the unusual endothermic peak of $Au_{70}Cu_{5.5}Ag_{7.5}Si_{17}$ metallic glass under a very high heating rate using a flash differential scanning calorimetry (FDSC). They ascribed this endothermic process to the occurrence of the amorphous phase.

Although the direct observation of the two-step SSPT in real material is still scarce, the solid-state amorphization (SSA) [24,25], which is the leading step in a CAC two-step SSPT, has long been recognized. As early as the 1980s, it has been found that the amorphous phase produced by irradiation appears to be structurally similar to the same material quenched rapidly from the melt [24,26,27]. It was soon found that high pressure [28–31], severe plastic deformation [32] or mechanical alloying [33] can lead to an amorphous structure. To understand the fundamental cause of SSA, Johnson et al. [34] discussed the similarity between amorphization and melting and proposed a polymorphic phase diagram to rationalize the critical conditions of SSA, under which atomic diffusion is still slow but a crystalline lattice has become mechanically unstable. With this idea, Johnson et al. [34] examined the Nb—Pd alloy in 1993 and showed the evidence of elastic instability based on the measurement of the Debye temperature and the mean square displacement of atoms from their ideal crystallographic sites. It should be noted that the amorphous phase thus formed would spontaneously transform to a crystalline phase, accomplishing a CAC two-step process. Therefore, even the SSA does occur, the amorphous phase cannot be kept at room temperature for direct observation [34].

The early investigation of the SSA indicates that the kinetic pathway of the SSPT passing an amorphous state can be conceptualized. But it is still difficult to demonstrate it in experimentation. In our attempt to measure the variation of Young's modulus with temperature of a duplex stainless steel by using the Impulse Excitation Technique (IET), a precipitous sudden drop of the Young's modulus associated with a surge of

internal friction was observed, which could be evidence of CAC two-step process. In the following, such an unexpected result is reported and the rationale for attributing it to the two-step SSPT is elaborated.

2. Material

The nominal chemical composition of the DSS is 15Cr-2Ni-2Al-12Mn, which is prepared by arc melting and copper-mold quenching, as shown in Fig. 1. The actual chemical composition is determined by an Energy Dispersive X-Ray spectroscopy (EDX) equipped in a Scanning Electron Microscope (SEM, JEOL Model JSM-6490), which is listed in Table 1. The variation of the composition from ingot-1 to ingot-2 is attributed to the slight variation in the preparation of pure metals as well as the evaporation of low-boiling-point metal such as Mn. In the sample preparation, the iron manganese alloy is used to reduce the evaporation of manganese. If the melt is slowly cooled, the austenite (γ) phase will be the main phase at the room temperature. However, the rapid quenching results in about 70% ferrite (δ) phase in the as-cast alloy, which is much higher than the equilibrium phase constituent. As a result, the driving force for the δ to γ SSPT is significant. The as-cast sample is wire-cut into plates, some of which are cold-rolled with different thickness reduction rate. Metallographs of the as-cast and cold-rolled samples after electrolytically etched in 15 wt% KOH solution are shown in Fig. 2(a) and (b), respectively. In Fig. 2, the duplex structure of δ and γ phase can be well discerned, in which the grey region corresponds to the δ phase and the bright region is the γ phase. The composition of the cold-rolled specimen has also been examined using an atom probe tomography (APT, CAMECA LEAP 5000 HR). The specimen is analyzed at 50 K in the voltage mode with a pulse repetition rate of 200 kHz, a pulse fraction of 20%, and an evaporation detection rate of 0.5% atom per pulse. Imago Visualization and Analysis Software (IVAS) version 3.8 is used for creating the 3D reconstructions and data analysis. The results as shown in Fig. 3 indicate a uniform distribution of the five constituent elements in the 40 nm × 40 nm × 150 nm needle. No apparent elemental segregation or precipitation of secondary phase can be discerned.

3. Experimental

The Young's modulus (E) can be measured by various approaches [35]. In this work, we probe the frequency f and decay rate β (namely assume a vibrational response in the form of $\exp(-\beta t)\sin(2\pi ft + \varphi)$) of the specimen based on the Impulse Excitation Technique (IET, IMCE RFDA HT1600) [36], as illustrated in Fig. 4. In each measurement, the specimen was tied using thin PtRh wires at the nodes, which are the stationary points of the fundamental flexible vibration mode of a free-standing beam. The whole fixture was then put into the dedicated IET furnace and nitrogen gas was continuously purged to minimize the effect of oxidation. During heating with the rate of 15 °C/min, the specimen was hit at the middle span every 15 s by a pneumatically actuated tapper, and the sound generated by the free vibrating specimen was collected by a sound collection system above the middle span of the sample, which consists of a ceramic bar inside the furnace for sound transmission and a high-precision microphone outside the furnace for recording. The Young's modulus, which is proportional to the square of frequency f, was calculated according to the American Society for Testing and Materials (ASTM) standard 1876 [37]. And the decay rate β was determined from the Half Width at Half Maximum (HWHM) of the signal, which describes the internal friction of the material, given as $Q^{-1} = \beta/\pi f$.

The in-situ X-ray diffraction (XRD) patterns in a heating process were determined by the PANalytical Empyrean X-ray diffractometer with Cu Kα radiation. In order to ensure a swift scan in the continuous heating process, the 2θ angle only ranges from 35 to 55° to capture the neighboring γ(111) and δ(011) peaks. Since the two peaks are close, the Peak Height Ration (PHR$_{δ/γ}$) can be used to represent the
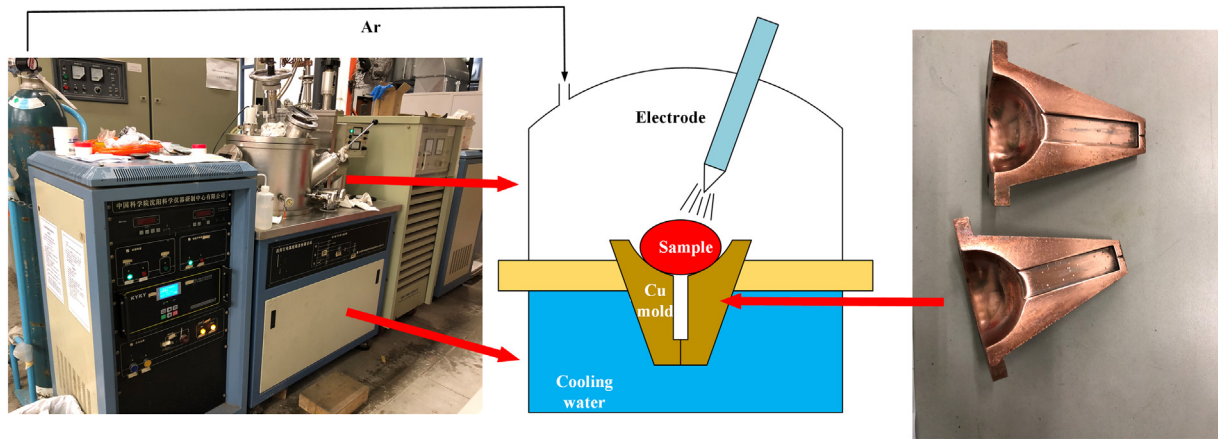
Fig. 1. Photographs of the arc furnace and copper molds with a schematic of the setup.

ratio of volume fractions of the ferrite and austenite phase [38]. The thermal behavior was investigated using a Differential Scanning Calorimeter (DSC, Mettler Toledo TGA/DSC3+) with a resolution of 100 μW. Both as-cast and cold-rolled samples were heated at the rate of 15 °C/min (same as that of IET measurements) in the nitrogen atmosphere.

4. Results

4.1. Anomalous drop of Young's modulus

The temperature-dependent Young's moduli of duplex stainless steels (DSSs), cold-rolled with various thickness reduction, are shown in Fig. 5(a) (the samples are cut from ingot-1 as shown in Table 1). If the DSS is not rolled, the Young's modulus decreases almost linearly with temperature in the range of room temperature (RT) to 400 °C. The E-T curve then becomes concave in the temperature range of 400–870 °C and convex again at the inflection point of about 870 °C. With the increase of the thickness-reduction rate through cold rolling at RT, the temperature of the inflection point remains almost unchanged, but the inflection becomes increasingly sharper, more akin to a Glass-Transition-Like (GTL) phenomenon. For an analogy, Fig. 5 (b) shows the E-T curves of the Fe-based ($Fe_{41}Co_7Cr_{15}Mo_{14}C_{15}B_6Y_2$ [39]) and Cu-based ($Cu_{60}Zr_{20}Hf_{10}Ti_{10}$ [40]) metallic glasses examined by IET, which also exits the concave to convex transition at the glass transition point. When the temperature goes higher than the GTL point (T_{GTL}), the unexpected Sudden Drop of Modulus (SDM) occurs at a critical temperature T_{SDM} ($\approx$ 950 °C) for the DSS specimens after 50% and 70% thickness reduction. This drop amounts to about 28% loss of the measured modulus, indicating that the stiffness of a substantial portion of material becomes suddenly very small or undetectable. The comparison of the as-cast and cold-rolled DSS indicates that the severe plastic deformation is a necessary condition for observing SDM. The plastic deformation in the 30% rolled DSS is probably inadequate to bring about a large SDM, though a small sudden reduction of modulus can also be discerned at about 1000 °C. It is further noted that after the SDM the moduli of the 50% and 70% rolled DSS increase slowly with the temperature, which is also unexpected and against the intuition that the modulus should decrease as temperature increases. The GTL and SDM phenomena are not only exhibited by the variation of

Young's modulus but also associated with the surge of internal friction Q^{-1}, as shown in the inset of Fig. 5(a). It is noted that the internal friction of the cold-rolled DSS starts a gradual increase from about 400 °C, seemingly levels off at 600–800 °C, then surges precipitously to a very large magnitude (~0.25) at another critical temperature ($T_{QMax} \approx 910$ °C) lower than T_{SDM} ($\approx$950 °C), and subsequently reduces to the magnitude (~ 0.05) that is same as that of the as-cast DSS at the higher temperatures.

To confirm the repeatability of the above results, we repeat the experiment using specimens cutting from another ingot (ingot-2 as shown in Table 1). The measured temperature dependences of Young's modulus and decay rate are similar to those of Fig. 5(a), except that its T_{SDM} is slightly lower of about 930 °C, which is probably due to the variation of composition (say the concentration of Mn). Fig. 5(c) shows the variations of E and β of the sample cut from the second ingot during aging at T_{SDM} + 5 °C. It is noted that the modulus recovers quickly in the first 60 min and then slowly approaches the value that can be expected by extrapolating the E-T curve before the SDM. Correspondingly, the decay rate β decreases quickly in the first 60 min and then approaches a plateau.

While the severe plastic deformation of DSS is one of the main causes of the SDM as shown in Fig. 5(a), the role of SSPT should also be clarified. Therefore, we examined the conventional single-phase stainless steels for comparison. Fig. 6(a) shows the E-T curves of the as-received and 70% cold-rolled austenitic (AISI 304) and ferritic (AISI 430) stainless steels. SSPT does not occur in the austenitic stainless steel over the examined temperature range. Therefore, both E-T curves, pertaining to the as-received and cold-rolled austenite stainless steels, respectively, show a rather smooth decrease — the SDM does not occur. It is noted that the slope of the E-T curve of the cold-rolled austenite stainless also changes at the temperature between 400 °C and 700 °C, which should be associated with dynamic recovery occurring in this temperature range. For the cold-rolled ferritic stainless steel, the phenomenon is akin to that of DSS, though less remarkable. Both the GTL phenomenon and the SDM can be observed, and the latter also occurs at the temperature about 950 °C. According to the phase diagram shown in Fig. 6(b) [41], the ferrite-to-austenite transformation in this ferritic 430 stainless steel does occur in the temperature range of 840–1270 °C, which suggests that SSPT is another necessary condition for the SDM. In addition, the variations of Q^{-1} for the two single-phase stainless steels after the same 70% rolling are also plotted in the inset of Fig. 5(a). It is noted that the cold-rolled ferritic 430 steel also exhibits a surge of internal friction, though less remarkable comparing with the results of the cold-rolled DSS. But the internal friction of cold-rolled the austenitic 304 steel remains very small in the whole temperature range. These results corroborate that SSPT is the reason for the surge of internal friction.

Table 1
The specific chemical compositions of DSS (wt%).

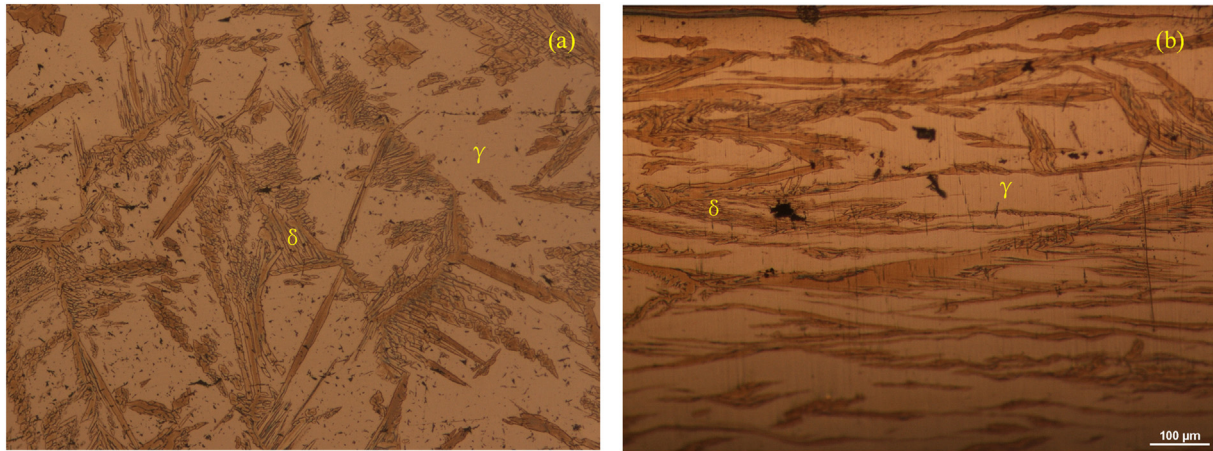| Element	Fe	Cr	Ni	Al	Mn
wt% of ingot-1	Balance	14.83	1.62	2.73	11.65
wt% of ingot-2	Balance	16.18	1.62	1.90	12.96

Fig. 2. Metallographs of the (a) as-cast and (b) cold-rolled DSS specimens, in which the grey region corresponds to the δ phase and the bright region is the γ phase.

4.2. Kinetics of ferrite-to-austenite transformation based on in-situ XRD

The TTT diagrams of both the as-cast and 70% rolled DSSs based on water-quenched specimens, have been obtained in our previous work [10] and listed in Fig. 7, showing that the temperature range of ferrite-to-austenite transformation covers both the GTL and the SDM temperatures. To have a more direct comparison, the in-situ high-temperature X-Ray Diffraction (XRD) patterns of both as-cast and 70% cold-rolled DSS specimens under the same heating rate are shown in Fig. 8. The $PHR_{\delta/\gamma}$ of the diffraction peaks pertaining to γ(111) and δ(011) (the error bar is to account for the background noise) is normalized by the corresponding RT value, giving rise to a rough indication of the variation of phase content. It is noted that the phase transformation in the as-cast sample lags behind that in the cold-rolled one. The temperatures corresponding to the GTL point, the maximum Q^{-1} and the SDM are all marked in Fig. 8(a). It is noted that the temperature of the GTL point is slightly higher than the commencing temperature of SSPT and that the SDM occurs when SSPT has almost finished. The small peak at about $2\theta = 39°$ in the XRD patterns of the as-cast DSS has been indexed as σ phase according to a dedicated study of ternary Fe-Cr-(Ni, Co) σ intermetallics [42]. While as the figure shows, its fraction is so small in the as-cast sample and almost disappears in the cold-rolled sample.

4.3. Results of DSC and microstructure observation

A possible explanation of the observed SDM is the melting of some last solidified region. Therefore, the thermal behavior of the DSS in the temperature region of GTL and SDM is monitored using the DSC. The Heat Flow (HF) curves of the as-cast and 70% cold-rolled samples resulted from a continuous heating at the rate 15 °C/min (same as that of IET experiment) are plotted in Fig. 9(a). It is noted that the cold-rolled specimen exhibits a weak exothermic hump in the temperature range of 200–600 °C in comparison with the as-cast specimen, which should be ascribed to dynamic recovery. However, in the temperature range of GTL and SDM (from 800 °C to 1000 °C), the DSC curve of the cold-rolled specimen is featureless, except that the cold-rolled specimen is more endothermic than the as-cast one, indicating a more radical δ to γ phase transformation, which is consistent with the result of in-situ XRD as shown in Fig. 8. We further annealed the specimens at $T_{SDM} + 5$ °C for 2 h (corresponding to the result of Fig. 5(c)) in the DSC furnace and record the heat flow of the co-rolled and as-cast specimens. Fig. 9(b) shows the difference of the heat flow (D_{HF}) between the cold-rolled and as-cast samples ($D_{HF} = HF_{cold-rolled} - HF_{as-cast}$), which is positive, indicating an exothermic behavior. The heat continuously releases with the magnitude between 0.2 and 0.3 W/g during the two-
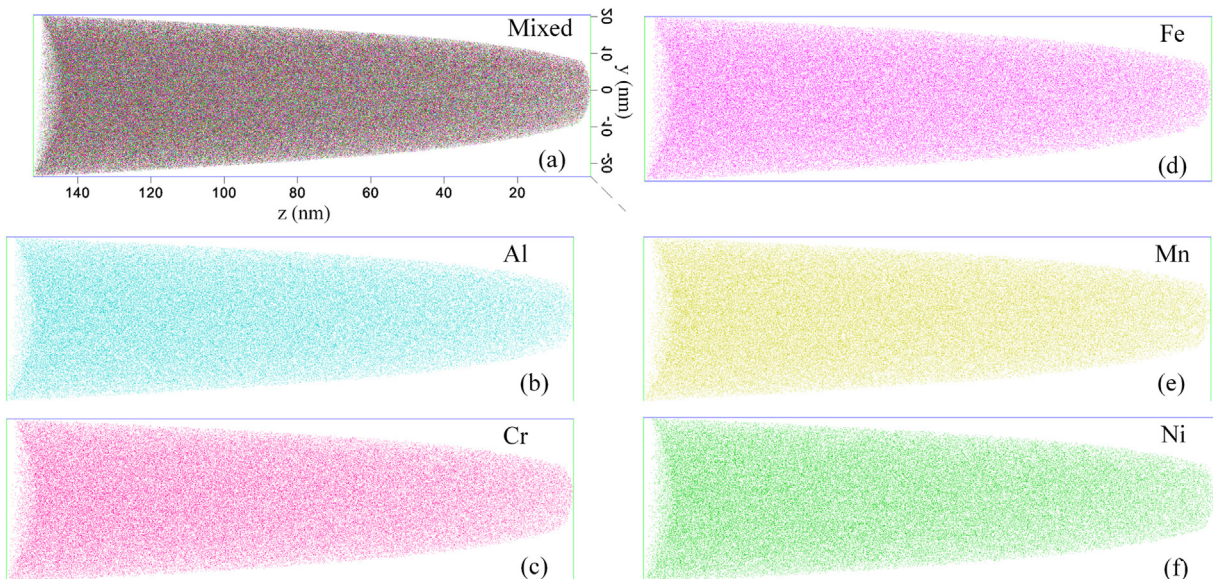

Fig. 3. Elemental maps of (a) the mixed distribution and (b-f) the five individual elements in a room-temperature 70% cold-rolled DSS specimen.
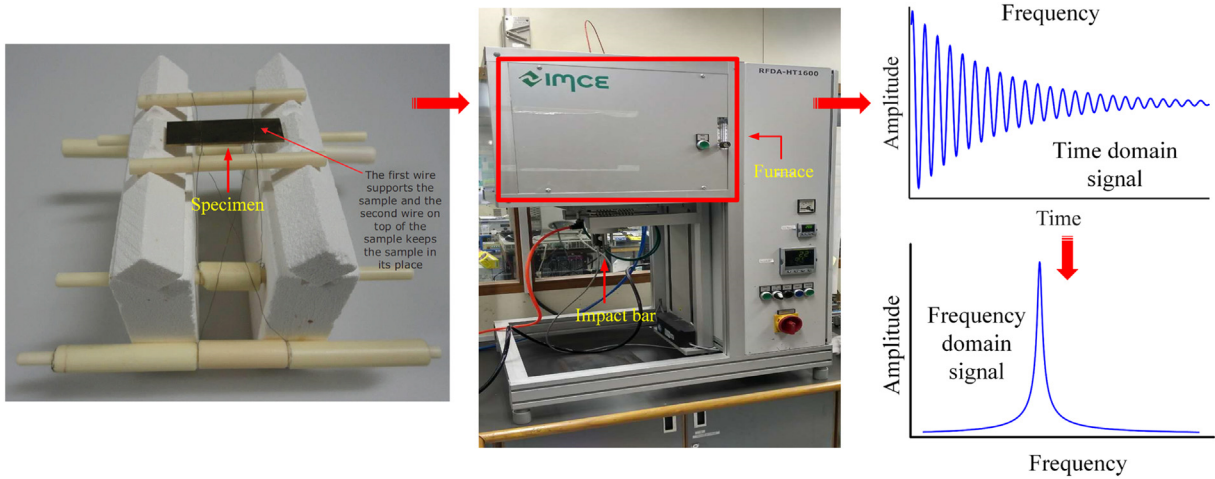
Fig. 4. The specimen, fixture, furnace and the obtained sound signal in an IET experiment.

hour annealing, which is accompanied with the continuous increase of Young's modulus resulted from the IET measurement, as shown in Fig. 9(b). It is worth stressing that although the δ-to-γ phase transformation is endothermic as shown in Fig. 9(a), the increase of Young's modulus after the sudden drop is associated with an exothermic process. This is an indication of the occurrence of an intermediate phase during the δ-to-γ transformation.

Microstructure observation under TEM however does not render any clue of the intermediate phase that can be associated with the SDM and the exothermic process after the SDM. Fig. 10(a-c) shows the microstructures of the 70% cold-rolled specimens which were water quenched after annealing at 750, 850 and 950 °C for 30 min, respectively. It is observed that the grain size increases with the annealing temperature and that those "dirty" grains containing a large number of

dislocations are generally δ phase. Correspondingly, those relative "clean" grains are γ phase that nucleated from the dislocated δ matrix, as confirmed by the selected area electron diffraction (SAED) pattern in Fig. 10(b) and (c). These newly-formed γ grains appear to be lath-shaped at the lower temperature (750 °C) and become more equiaxial at the higher temperature. This is the result of the competition between the interfacial misfit energy and the volumetric free energy. At the lower annealing temperature, the residual stress caused by the eigenstrain (due to lattice misfit) is significant and heterogeneous, so that the grain would grow along the direction that minimizes the total free energy the most quickly. While at higher annealing temperature, the effect of eigenstrain is weakened due to the enhanced stress relaxation. Therefore, the grains would appear to be more equiaxial. The fraction of γ grains also increases with the annealing temperature, because
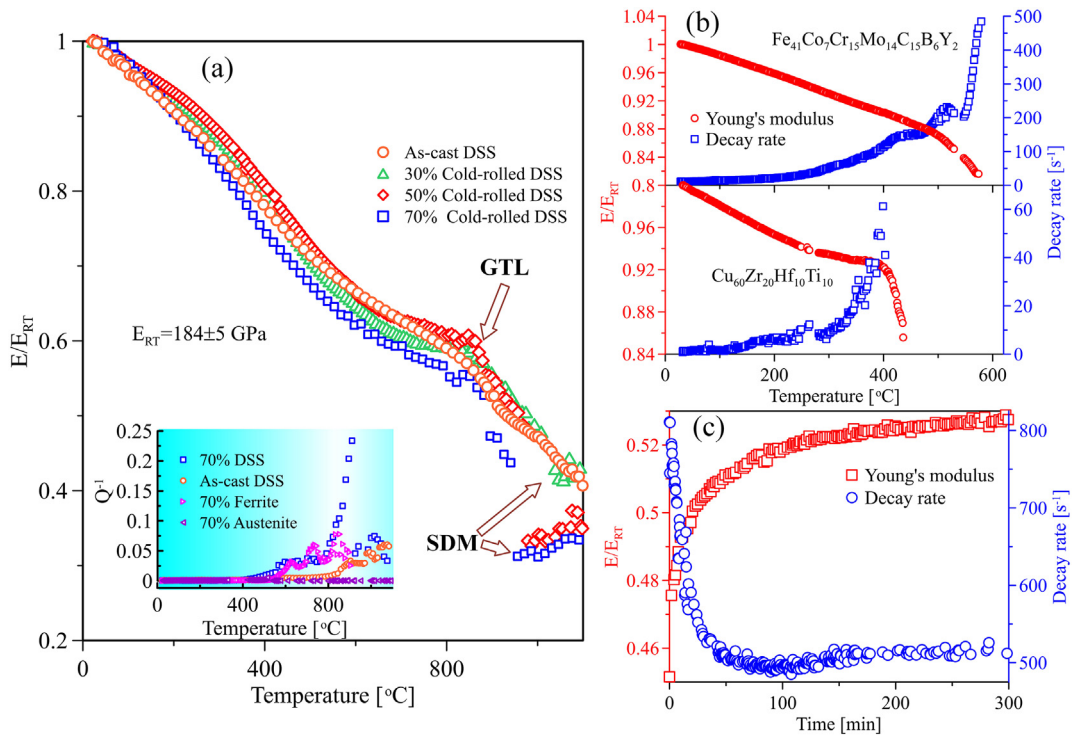

Fig. 5. (a) The variation of Young's modulus of as-cast and cold-rolled DSS with temperature under a heating rate of 15 °C/min. The bottom inset is the internal friction of the as-cast and cold-rolled DSS as well as the 70% cold-rolled ferritic and austenitic stainless steels; (b) The temperature dependence of Young's modulus and decay rate of the Fe-based ($Fe_{41}Co_7Cr_{15}Mo_{14}C_{15}B_6Y_2$) and Cu-based ($Cu_{60}Zr_{20}Hf_{10}Ti_{10}$) metallic glass measured by IET; (c) The measured Young's modulus and decay rate of the 70% cold-rolled DSS annealed at $T_{SDM} + 5$ °C.
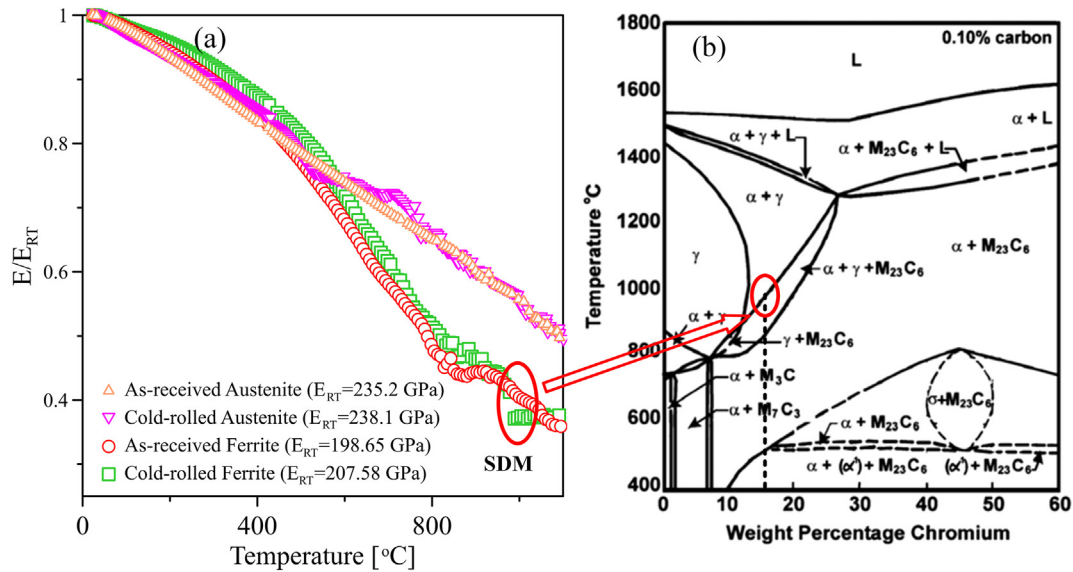
Fig. 6. (a) The measured *E-T* curves of the as-received and cold-rolled ferritic (AISI 430) and austenitic (AISI 304) stainless steels; (b) The phase diagram of chromium steel [41].

the kinetics of the δ-to-γ phase transformation becomes more speedy. However, these observations only confirm the δ-to-γ SSPT. We cannot find any microstructural features that can be associated with the SDM phenomenon.

5. Discussion

Based on the DSC result as shown in Fig. 9, the SDM is not caused by the early melting of the last solidified regions. It would then be desirable to find microstructures that can lead to the SDM. However, the quenched specimens from the temperature range of 700–1000 °C only contains crystalline δ and γ phases [11] as shown in Fig. 10. Apparently, the microstructure responsible for the SDM is transient and disappears during cooling. The small peak at about $2\theta = 39°$ in the XRD patterns of the as-cast DSS has been indexed as σ phase. In our previous study [4], we have found that the content of σ phase is no more than 1% after one-hour annealing at the temperature between 750 and 1050 °C which agrees with the results in Fig. 8. It should be noted that the σ phase is a crystalline phase, which is not likely the reason for the 28% drop in Young's modulus at the temperature of about 950 °C. In addition, based on the comparison of the XRD patterns as shown in Fig. 8, the σ phase is indiscernible in the cold-rolled samples; therefore, the SDM found in the cold-rolled samples cannot be ascribed to the formation of σ phase. Therefore, we can only conceive what happened in the

materials based on some theoretical considerations. In the following, we argue that the cause of the SDM and the corresponding surge of the decay rate is the occurrence of the transient amorphous phase during the δ→γ transition. And the most important evidence leading to such an argument is the anomalously large internal friction before the SDM ($T_{QMAX} < T_{SDM}$), being about 0.25 as shown in the inset of Fig. 5(a).

It is noted that the internal friction induced by dislocation activities are not able to account for such a large Q^{-1}, which can be confirmed based on the single-phase stainless steels (inset of Fig. 5(a)). For glasses, the transition from a solid-like (Kelvin-Voight-type) to a liquid-like (Maxwell-type) behavior can bring about a precipitous increase of damping at a very narrow temperature range (near T_g) owing to the quick reduction of viscosity. Noting that the definition of internal friction Q^{-1} becomes ill-posed owing to the change of viscoelastic behavior after glass transition (The definition $Q^{-1} = \beta/\pi f$ is based on the Kelvin-Voigt picture), we plot directly the decay rate β in Fig. 11(a-d) for the 70% cold-rolled DSS, together with some chalcogenide, borosilicate and metallic glasses respectively, for comparison, which were all measured by the IET system. It is noted that the measured β of these glasses are all much smaller than the maximum β (~ 2000 s^{-1}) of the 70% cold-rolled DSS. Measurements at higher temperatures for these glasses are no longer possible based on IET because the further reduction of viscosity leads to a quick dissipation of the energy input – the beam does not vibrate at all after an impulse.
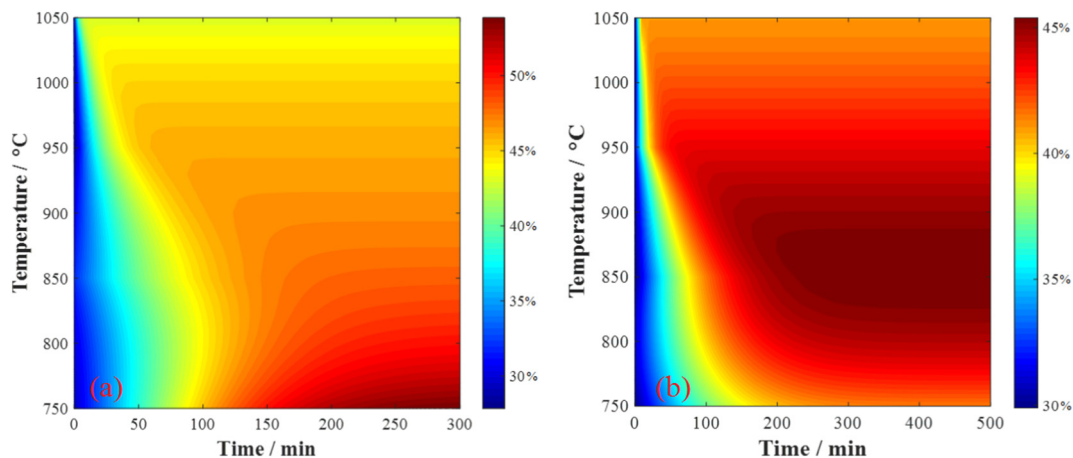

Fig. 7. TTT diagrams of austenitic volume fraction of (a) as-cast and (b) cold-rolled samples [4].
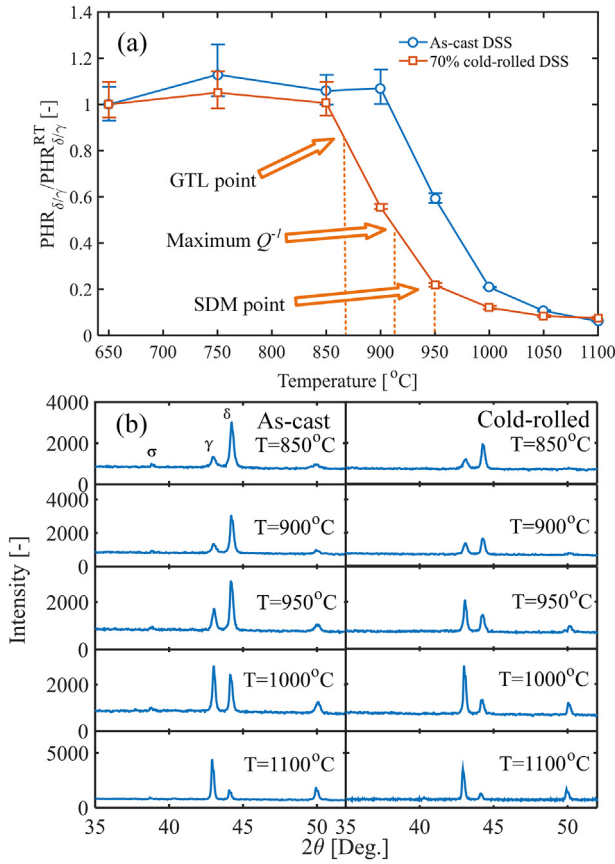
Fig. 8. The in-situ (continuous heating) XRD patterns of the as-cast and cold-rolled DSS. In order to ensure a swift scan in the continuous heating process, the 2θ angle only ranges from 35 to 55° to capture the neighboring γ(111) and δ(011) peaks. (a) The temperature dependence of the peak ratio of γ(111)/δ(011) normalized by the room-temperature magnitude; (b) The XRD patterns of the as-cast and cold-rolled samples at different temperatures.

The question is then why the cold-rolled DSS specimen can exhibit much larger decay rate β than those of glasses. To answer this question, let us compare the dynamic behavior of two cases of viscoelastic beams based on finite element simulation. The dynamic response of a beam is

simulated using a commercial finite element (FE) package ABAQUS. The FE model of the beam is a plane-strain two-dimensional model with the size identical to the sample used in the IET testing: $40.66 \text{ mm} \times 1.22 \text{ mm} \times 14.46 \text{ mm}$. The two points at the bottom of the beam model, which coincide with the stationary points of the fundamental flexible vibration mode of a free-standing beam, are fixed as shown in the inset of Fig. 12. The bottom mid-point of the beam is subjected to a square impulse within 0.1 ms to excite the vibration, and the displacement of this point is collected to represent the vibration signal obtained in an IET experiment.

In Case I, the material of the beam is a Maxwell solid with Young's modulus $E = 100 \text{ GPa}$ and viscosity $\eta_M = 3 \times 10^6 \text{ Pa} \cdot \text{s}$. The constitutive relation can be express as:

$$\sigma = E\varepsilon_0 \exp\left(-\frac{t}{\tau_M}\right) + E \int_0^t \exp\left(-\frac{t-t'}{\tau_M}\right)\dot{\varepsilon}(t')dt' \qquad (1)$$

in which σ and ε denote the normal stress and normal strain along the axial direction, respectively, and ε_0 stands for the initial strain. $\tau_M = \eta_M/E$ is the relaxation time.

In Case II, the beam is composed of 70% Kelvin-Voigt matrix ($E = 100 \text{ GPa}$, $\eta_K = 10^2 \text{ Pa} \cdot \text{s}$) and 30% Maxwell inclusions ($E = 100 \text{ GPa}$, $\eta_M = 3 \times 10^6 \text{ Pa} \cdot \text{s}$). The constitutive relation of the Kelvin-Voigt solid is:

$$\sigma = E\varepsilon + \eta_K\dot{\varepsilon} \qquad (2)$$

The dynamic response of the beam is simulated using the solver ABAQUS/Explicit [43], which solves the following kinetic equations from step i to $i + 1$ with a small time increment $\Delta t_{(i)}$:

$$\dot{\mathbf{u}}\left(i+\frac{1}{2}\right) = \dot{\mathbf{u}}\left(i-\frac{1}{2}\right) + \frac{\Delta t_{(i+1)} + \Delta t_{(i)}}{2}\ddot{\mathbf{u}}_{(i)} \qquad (3)$$

$$\mathbf{u}_{(i+1)} = \mathbf{u}_{(i)} + \Delta t_{(i+1)}\dot{\mathbf{u}}\left(i+\frac{1}{2}\right) \qquad (4)$$

in which $\mathbf{u}$, $\dot{\mathbf{u}}$, and $\ddot{\mathbf{u}}$ are displacement, velocity and acceleration vectors of an integration point, respectively. The acceleration at step i is computed by:

$$\ddot{\mathbf{u}}_{(i)} = \mathbf{M}^{-1}\left(\mathbf{P}_{(i)} - \mathbf{I}_{(i)}\right) \qquad (5)$$
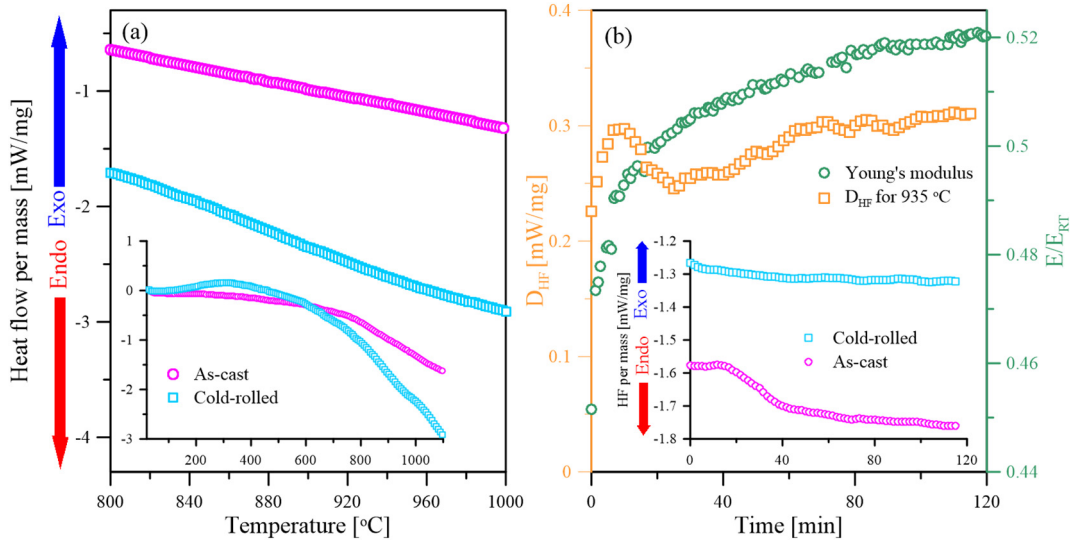

Fig. 9. (a) The heat flow curves of the as-cast and 70% cold-rolled DSS samples with a heating rate of 15 °C/min in the temperature region of 800 °C–1000 °C. The inset is the DSC curves of these two samples in the whole measurement temperature range (RT to 1100 °C); (b) The D_{HF} between the as-cast and 70% cold-rolled samples annealing at $T_{SDM} + 5$ °C, and the corresponding Young's modulus of the 70% cold-rolled one. The inset shows the DSC curves of the as-cast and cold-rolled samples at $T_{SDM} + 5$ °C.
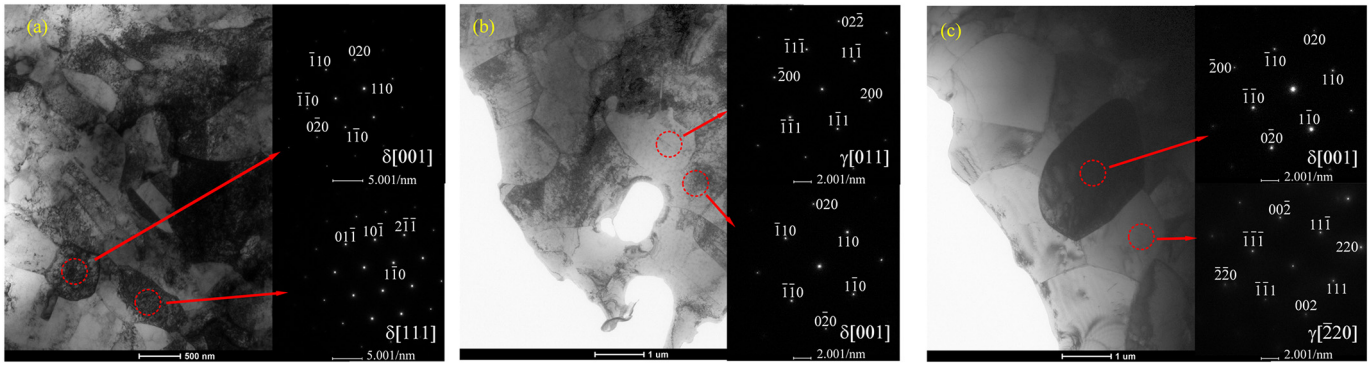
Fig. 10. Bright-field TEM images and the selected area electron diffraction (SAED) pattern of the cold-rolled specimens annealed at (a) 750 °C, (b) 850 °C and (c) 950 °C for 30 min and then water-quenched.

where the **M** is the mass matrix, **P** stands for the applied load, and **I** is the internal force calculated from the constitutive relations (Eqs. (1) and (2)) and the stress equilibrium equation:

$$\mathbf{I}_{(i+1)} = \nabla \cdot \boldsymbol{\sigma}_{(i)} \qquad (6)$$

The simulation results of Cases I and II are shown in Fig. 12(a). It is noted that for Case I, representing the glass beams at the temperature
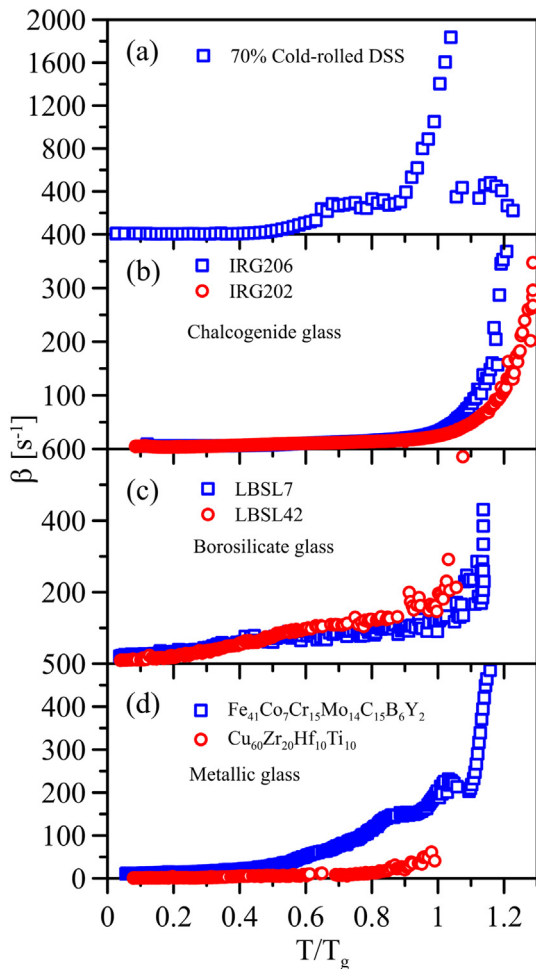

Fig. 11. Decay rate β of the (a) 70% cold-rolled DSS, (b) chalcogenide glass (IRG206 and IRG202), (c) borosilicate glass (LBSL7 and LBSL42) and (d) metallic glass (Fe- and Cu-based) versus temperature. For glasses, the temperature is normalized by their glass transition temperature (T_g), respectively; for DSS, the temperature is normalized by the GTL point (915 °C).

higher than T_g, the mid-point impulse cannot bring about vibration when the Maxwell viscosity is 3×10^6 Pa·s. For Case II, the beam vibrates after impact since the Maxwell inclusion of the same viscosity is surrounded by the Kelvin-Voigt Matrix. More importantly, the 30% Maxwell inclusion can still be dynamically stressed, and their transient elastic response still contributes to the overall stiffness, since the effective modulus calculated from the vibration frequency is still very close to 100 GPa. The energy dissipated by the inclusions then results in a huge decay rate more than 1000 s^{-1}. This composite beam model explains the large decay rate at the temperature lower than the SDM point as shown in Fig. 11(a). At this temperature, the transient amorphous phase still partly contributes to the overall stiffness in the IET experiment and at the same time brings about the very large decay rate. Upon the further increase of temperature, the viscosity of the transient amorphous phase becomes so low that it is no longer loadable at the vibration frequency (i.e., becomes liquid-like), leading to the sudden drop of modulus (Fig. 5(a)) as well as the sudden drop of decay rate (Fig. 11 (a)).

We would like to clarify that the rapid drop of the internal friction as shown in the inset of Fig. 5(a) is not due to the reduction of the volume fraction of the amorphous inclusion. Instead, it is attributed to the rapid reduction of the viscosity or relaxation time of the amorphous phase. Qualitatively, one can imagine that if the relaxation time of amorphous inclusion is much less than the vibration period of the beam, the contribution of the inclusions to the vibrational response of the beam would disappear. In this case, the composite beam can be simplified as a porous beam because the disturbance to the inclusion diminishes too quickly. To be more quantitative, the case of the beam with the Maxwell inclusion (with the same volume fraction in Case II) with the viscosity of 1 $\times 10^5$ Pa·s has been simulated, as shown in Fig. 12(b). The result shows that the decay rate resulted from the case with the lower inclusion viscosity of 10^5 Pa·s becomes also much lower than that of the case with inclusion viscosity 3×10^6 Pa·s. It should be noted that viscosity reduces very precipitously with temperature. As a rule of thumb, the viscosity of iron-based metallic glass reduces one order of magnitude when the temperature increases about 20 °C. For the internal friction data of the 70% rolled DSS as shown in the inset of Fig. 5(a), from the highest point of the inter friction to the point next to it, the temperature difference is more than 30 °C. Between them, the viscosity of the amorphous phase may have reduced more than one order of magnitude. And this is the reason for the sudden drop of internal friction in the narrow temperature range. Instead, if the temperature is kept constant and the viscosity of the amorphous phase does not change, we did obtain a gradual reduction of the internal friction (or decay rate) as shown in Fig. 5(c), which is due to the gradual reduction of the metastable amorphous phase.

We shall finally rationalize the role of plastic deformation because the as-cast specimen does not exhibit the SDM phenomenon. Although the $\delta \rightarrow \gamma$ transformation occurs in both as-cast and cold-rolled DSS
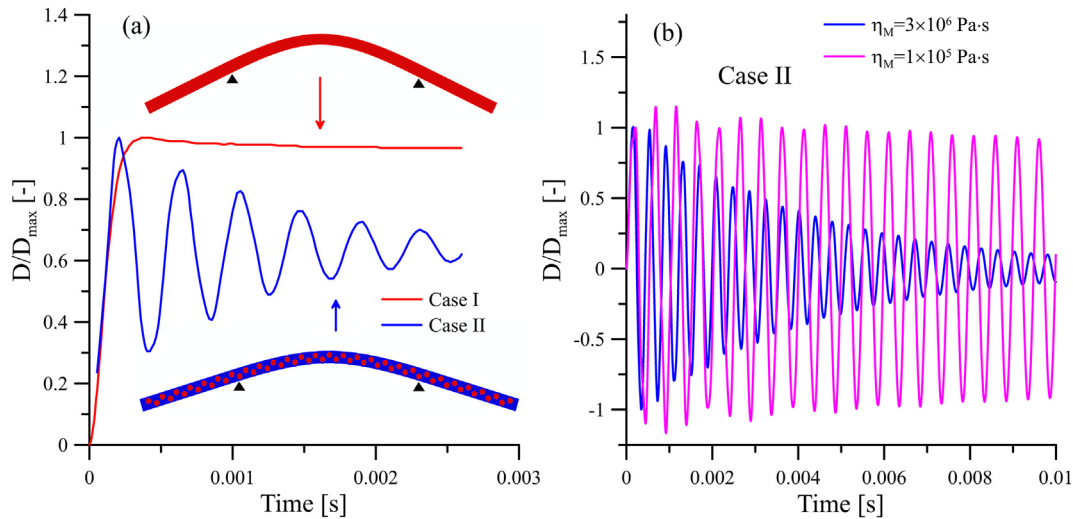
Fig. 12. Normalized displacements of (a) the pure Maxwell beam (Case I) and the composite beam with Kelvin-Voigt matrix and Maxwell inclusions (Case II), and (b) the composite beam with different viscosity of the inclusions.

specimens, the severe plastic deformation is a necessary condition for generating the transient amorphous phase that causes SDM. In the as-cast specimen, the free energy of both the δ and γ phases are much lower than the amorphous phase that the diffusional δ→γ SSPT occurs without non-crystallizing. However in the cold-rolled specimen, the free energy of the mother δ phase is increased to be comparable with that of the amorphous phase, one may expect a quick reduction of free energy by amorphization because the dislocated lattice has been elastically unstable, which leads to the SDM. This facilitating of the plastic deformation is confirmed by the colloidal sphere experiment [5]. Besides, in early works, it is corroborated that the plastic deformation itself could lead to the amorphization, such as the observation in the nano-crystalline NiTi micropillars under uniaxial compression [44]. Due to the metastability of the amorphous phase, the crystallization and diffusion occur successively, further bringing the slow increase of the modulus and recovery of the decay rate in the heating (Fig. 5(a)) and annealing (Fig. 5(c)) processes.

Due to the compositional difference as shown in Table 1, the viscosity-temperature relation of the amorphous phase in the two samples could be disparate, leading to different SDM temperatures. This kind of variation in viscosity due to slight composition change is very common in metallic glasses. For example, in a list of iron-based metallic glasses reviewed free-standing beam [45], one can find the subtle dependence of the glass transition temperature T_g (at which viscosity is 10^{12} Pa·s) on composition. For the DSC curves, there is indeed a small endothermal peak near 950 °C for the cold-rolled sample, as shown in Fig. 9(a). Based on the proposed CAC two-step transformation, this endothermal peak could be correlated to the formation of a substantiated amount of amorphous phase at the temperature range, which causes SDM.

6. Conclusions

Using the impulse excitation technique and with a normal heating rate, we find the glass-transition-like variation and the sudden drop of the Young's modulus at two temperatures respectively in the severely cold-rolled duplex stainless steel. And the absence of these phenomena in the as-cast sample and other single-phase alloys suggests the complexity of the SSPT in the dual-phase plastically deformed alloy. Even though it is difficult to observe the transition directly using microscopy, the abrupt inflection of the modulus-temperature curve, the precipitous surge of the decay rate, the sudden large drop of modulus and the gradual increase of modulus after SDM all evidence the existence of the transient amorphous phase during the SSPT collaterally. The DSC results

exclude the possibility of early melting and suggest that the slow recovery of the Young's modulus is associated with an exothermic process, which is also consistent with the notion that the transient phase, after causing the SDM, will transform to crystalline phases and release heat. Though our experimental results are based on the duplex stainless steel, the two-step SSPT could be universal in other multiphase alloys and therefore worthy of further exploration.

Data availability

The experimental data will be provided on request.

CRediT authorship contribution statement

Acknowledgements

References

[1] P.C. Chakraborti, M.K. Mitra, Microstructure and tensile properties of high strength duplex ferrite–martensite (DFM) steels, Mater. Sci. Eng. A 466 (2007) 123–133.

[2] Y.-J. Kim, L.S. Chumbley, B. Gleeson, Determination of isothermal transformation diagrams for sigma-phase formation in cast duplex stainless steels CD3MN and CD3MWCuN, Metall. Mater. Trans. A 35 (2004) 3377–3386.

[3] R. Magnabosco, Kinetics of sigma phase formation in a duplex stainless steel, Mater. Res. 12 (2009) 321–327.

[4] J. Wan, H. Ruan, J. Wang, S. Shi, The kinetic diagram of sigma phase and its precipitation hardening effect on 15Cr-2Ni duplex stainless steel, Mater. Sci. Eng. A 711 (2018) 571–578.

[5] Y. Peng, F. Wang, Z. Wang, A.M. Alsayed, Z. Zhang, A.G. Yodh, et al., Two-step nucleation mechanism in solid-solid phase transitions, Nat. Mater. 14 (2015) 101–108.

[6] X.-S. Yang, S. Sun, T.-Y. Zhang, The mechanism of bcc α' nucleation in single hcp ε laths in the fcc γ→hcp ε→bcc α' martensitic phase transformation, Acta Mater. 95 (2015) 264–273.

[7] Lenz LK, Heuer AH. Stress-induced transformation during subcritical crack growth in partially stabilized zirconia. Journal of the American Ceramic Society. 1982;65: C-192-C-4.

[8]   M. Cherkaoui, M. Berveiller, X. Lemoine, Couplings between plasticity and martens-
       itic phase transformation: overall behavior of polycrystalline TRIP steels, Int. J. Plast.
       16 (2000) 1215–1241.
[9]   W.D. Callister, D.G. Rethwisch, Materials Science and Engineering: An Introduction,
       Wiley, New York, 2007.
[10] J. Wan, H. Ruan, J. Wang, S. Shi, Exploiting the non-equilibrium phase transforma-
       tion in a 15Cr-2Ni-2Al-11Mn resource-saving duplex stainless steel, Mater. Des.
       114 (2017) 433–440.
[11] J. Wan, H. Ruan, S. Shi, Excellent combination of strength and ductility in 15Cr-2Ni
       duplex stainless steel based on ultrafine-grained austenite phase, Mater. Sci. Eng.
       A 690 (2017) 96–103.
[12] S. Pogatscher, D. Leutenegger, J.E. Schawe, P.J. Uggowitzer, J.F. Loffler, Solid-solid
       phase transitions via melting in metals, Nat. Commun. 7 (2016), 11113.
[13] S. Ebner, C. Suppan, A. Stark, R. Schnitzer, C. Hofer, Austenite decomposition and car-
       bon partitioning during quenching and partitioning heat treatments studied via in-
       situ X-ray diffraction, Mater. Des. 178 (2019), 107862.
[14] W. Ostwald, Studies on formation and transformation of solid materials, Z. Phys.
       Chem. 22 (1897) 289–330.
[15] H.J. Schope, G. Bryant, W. van Megen, Two-step crystallization kinetics in colloidal
       hard-sphere systems, Phys. Rev. Lett. 96 (2006), 175701.
[16] P. Tan, N. Xu, L. Xu, Visualizing kinetic pathways of homogeneous nucleation in col-
       loidal crystallization, Nat. Phys. 10 (2013) 73–79.
[17] L.E. Fox, D.R. Worsnop, M.S. Zahniser, S.C. Wofsy, Metastable phases in polar strato-
       spheric aerosols, Science 267 (1995) 351.
[18] J.D. Shore, D. Perchak, Y. Shnidman, Simulations of the nucleation of AgBr from so-
       lution, J. Chem. Phys. 113 (2000) 6276–6284.
[19] Y. Xu, D. Xu, X. Shao, E.-h. Han, Guinier-Preston zone, quasicrystal and long-period
       stacking ordered structure in Mg-based alloys, a review, Acta Metallurgica Sinica
       (English Letters). 26 (2013) 217–231.
[20] A.Y. Stroev, O.I. Gorbatov, Y.N. Gornostyrev, P.A. Korzhavyi, Solid solution decompo-
       sition and Guinier-Preston zone formation in Al-Cu alloys: a kinetic theory with an-
       isotropic interactions, Phys. Rev. Mater. 2 (2018), 033603.
[21] V.A. Phillips, Lattice resolution measurement of strain fields at Guinier-Preston
       zones in Al-3.0% Cu, Acta Metall. 21 (1973) 219–228.
[22] S. Auer, D. Frenkel, Prediction of absolute crystal-nucleation rate in hard-sphere col-
       loids, Nature 409 (2001) 1020–1023.
[23] S.E. Offerman, N.H. van Dijk, J. Sietsma, S. Grigull, E.M. Lauridsen, L. Margulies, et al.,
       Grain nucleation and growth during phase transformations, Science 298 (2002)
       1003–1005.
[24] W.L. Johnson, Thermodynamic and kinetic aspects of the crystal to glass transforma-
       tion in metallic materials, Prog. Mater. Sci. 30 (1986) 81–134.
[25] L. Zhang, H. Zhang, X. Ren, J. Eckert, Y. Wang, Z. Zhu, et al., Amorphous martensite in
       β-Ti alloys, Nat. Commun. 9 (2018) 506.
[26] K.C. Russell, Phase stability under irradiation, Prog. Mater. Sci. 28 (1984) 229–434.
[27] P.R. Okamoto, L.E. Rehn, J. Pearson, R. Bhadra, M. Grimsditch, Brillouin scattering and
       transmission electron microscopy studies of radiation-induced elastic softening,

[   ] disordering and amorphization of intermetallic compounds, J. Less Common Met.
       140 (1988) 231–244.
[28] C. Perottoni, J. Da Jornada, Pressure-induced amorphization and negative thermal
       expansion in ZrW2O8, Science 280 (1998) 886–889.
[29] Q. Hu, J.-F. Shu, A. Cadien, Y. Meng, W. Yang, H. Sheng, et al., Polymorphic phase
       transition mechanism of compressed coesite, Nat. Commun. 6 (2015) 6630.
[30] Y. Wang, J. Zhu, W. Yang, T. Wen, M. Pravica, Z. Liu, et al., Reversible switching be-
       tween pressure-induced amorphization and thermal-driven recrystallization in VO
       2 (B) nanosheets, Nat. Commun. 7 (2016), 12214.
[31] R. Hrubiak, Y. Meng, G. Shen, Microstructures define melting of molybdenum at
       high pressures, Nat. Commun. 8 (2017), 14562.
[32] He Y, Zhong L, Fan F, Wang C, Zhu T, Mao SX. In situ observation of shear-driven
       amorphization in silicon crystals. Nature nanotechnology. 2016;11:nnano.
       2016.166.
[33] C. Koch, O. Cavin, C. McKamey, J. Scarbrough, Preparation of "amorphous"Ni60Nb40
       by mechanical alloying, Appl. Phys. Lett. 43 (1983) 1017–1019.
[34] W. Johnson, M. Li, C. Krill III, The crystal to glass transformation in relation to melt-
       ing, J. Non-Cryst. Solids 156 (1993) 481–492.
[35] M. Tabellout, P.Y. Baillif, H. Randrianantoandro, F. Litzinger, T. Nicolai,
       et al., Glass-transition dynamics of a polyurethane gel using ultrasonic spectroscopy,
       dynamic light scattering, and dynamical mechanical thermal analysis, Phys. Rev. B
       51 (1995) 12295–12302.
[36] Z. Chen, U. Gandhi, J. Lee, R.H. Wagoner, Variation and consistency of Young's mod-
       ulus in steel, J. Mater. Process. Technol. 227 (2016) 227–243.
[37] ASTM, Standard Test Method for Dynamic Young's Modulus, Shear Modulus and
       Poisson's Ratio by Impulse Excitation of Vibration, West Conshohocken, ASTM Inter-
       national, 2007.
[38] J. Bednarcik, S. Michalik, V. Kolesar, U. Rütt, H. Franz, In situ XRD studies of
       nanocrystallization of Fe-based metallic glass: a comparative study by reciprocal
       and direct space methods, Phys. Chem. Chem. Phys. 15 (2013) 8470–8479.
[39] J. Shen, Q. Chen, J. Sun, H. Fan, G. Wang, Exceptionally high glass-forming ability of
       an FeCoCrMoCBY alloy, Appl. Phys. Lett. 86 (2005), 151907.
[40] X. Lin, W. Johnson, Formation of Ti–Zr–Cu–Ni bulk metallic glasses, J. Appl. Phys. 78
       (1995) 6514–6519.
[41] T. Lyman, Committee A, Metallography, Structures and Phase Diagrams, 8th ed
       American Soc. for Metals, 1973.
[42] J. Cieślak, J. Tobola, S.M. Dubiel, Site occupancies in sigma-phase Fe–Cr–X (X=Co,
       Ni) alloys: calculations versus experiment, Comput. Mater. Sci. 122 (2016) 229–239.
[43] I. Abaqus, Abaqus documentation, Version 6 (2014) 5–1.
[44] P. Hua, K. Chu, Q. Sun, Grain refinement and amorphization in nanocrystalline NiTi
       micropillars under uniaxial compression, Scr. Mater. 154 (2018) 123–126.
[45] C. Suryanarayana, A. Inoue, Iron-based bulk metallic glasses, Int. Mater. Rev. 58
       (2013) 131–166.